J. Fluid Mech. (2010), *vol.* 662, *pp.* 329–351.
doi:10.1017/S0022112010003319

CO_2 migration in saline aquifers. Part 1. Capillary trapping under slope and groundwater flow

C. W. MACMINN[1], M. L. SZULCZEWSKI[2] AND R. JUANES[2]†

[1]Department of Mechanical Engineering, Massachusetts Institute of Technology, Cambridge, MA 02139, USA

[2]Department of Civil and Environmental Engineering, Massachusetts Institute of Technology, Cambridge, MA 02139, USA

(Received 8 December 2009; revised 17 June 2010; accepted 18 June 2010; first published online 28 September 2010)

Injection of carbon dioxide (CO_2) into geological formations is widely regarded as a promising tool for reducing global atmospheric CO_2 emissions. To evaluate injection scenarios, estimate reservoir capacity and assess leakage risks, an accurate understanding of the subsurface spreading and migration of the plume of mobile CO_2 is essential. Here, we present a complete solution to a theoretical model for the subsurface migration of a plume of CO_2 due to natural groundwater flow and aquifer slope, and subject to residual trapping. The results show that the interplay of these effects leads to non-trivial behaviour in terms of trapping efficiency. The analytical nature of the solution offers insight into the physics of CO_2 migration, and allows for rapid, basin-specific capacity estimation. We use the solution to explore the parameter space via the storage efficiency, a macroscopic measure of plume migration. In a future study, we shall incorporate CO_2 dissolution into the migration model and study the importance of dissolution relative to capillary trapping and the impact of dissolution on the storage efficiency.

Key words: gravity currents, porous media

1. Introduction

Injection of carbon dioxide (CO_2) into geological formations is widely regarded as a promising tool for reducing global atmospheric CO_2 emissions (see e.g. Bachu, Gunter & Perkins 1994; Lackner 2003; Orr Jr 2004; Schrag 2007). To evaluate injection scenarios, estimate reservoir capacity and assess leakage risks, an accurate understanding of the subsurface migration of the plume of mobile CO_2 is essential. Much study has been done on this problem quite recently, including both theoretical modelling and numerical simulation. Numerical studies include Pruess & García (2002), Kumar *et al.* (2005) and Juanes *et al.* (2006), among many others; we review theoretical studies in more detail below. Here, we present a complete solution to a theoretical model for the subsurface migration of a plume of CO_2. The analytical nature of the solution offers insight into the physics of CO_2 migration and allows

† Email address for correspondence: juanes@mit.edu

for rapid, basin-specific estimation of, for example, migration distance and reservoir capacity.

1.1. *Saline aquifers and storage security*

Deep saline aquifers are among the geological formations well suited for CO_2 storage (see e.g. Bachu *et al.* 1994; Orr Jr 2004). These are permeable layers of, for example, limestone or cemented sand that are saturated with salty groundwater and bounded above and below by layers of much less permeable rock such as clay or anhydrite. Deep saline aquifers are located roughly 1–3 km underground, are thin relative to their in-plane dimensions, and are horizontal or weakly sloped. Many have a slow natural groundwater through-flow.

While the properties of CO_2 at aquifer conditions vary with temperature and pressure, the CO_2 will always be less dense and less viscous than the groundwater, making it buoyant and mobile in the aquifer. The injected plume of CO_2 will then spread upwards against the top boundary of the aquifer while migrating due to a combination of groundwater flow and aquifer slope.

Storage security (or, inversely, risk of leakage) is a primary concern. When both horizontal and upwards migration of mobile CO_2 are blocked by an impermeable layer, the CO_2 is said to be structurally trapped. Structural trapping is effective but unreliable, as the CO_2 remains mobile: a pre-existing well or the activation of a fault could lead to leakage into shallower formations. Several physical mechanisms serve to immobilize the CO_2 and thus increase storage security. The isolation and immobilization of small blobs of residual CO_2 in the pore space of the rock at the trailing edge of the plume is known as capillary trapping. Capillary trapping occurs in flow through a porous medium when a non-wetting fluid (here, CO_2) is displaced by a wetting one (here, groundwater). Capillary trapping is an ideal mechanism for the geological storage of CO_2 because the trapped gas is immobile and distributed over a large area, greatly decreasing the risk of leakage and enhancing the effectiveness of CO_2 dissolution (Kumar *et al.* 2005; Juanes *et al.* 2006). It is well known that both residual and mobile CO_2 will gradually dissolve into the groundwater: this offers excellent storage security, but CO_2 is only weakly soluble in groundwater and diffusion-driven dissolution acts on long time scales relative to plume migration. However, it is well known that dissolution is greatly enhanced by a Rayleigh–Bénard instability that drives convective mixing (Ennis-King & Paterson 2005). The combined effect of capillary trapping and dissolution will be considered in a future study. Once dissolved, CO_2 can precipitate onto the aquifer rock as carbonate mineral: this occurs over very long time scales, and is unlikely to influence plume migration.

1.2. *Previous study*

The injection and subsequent migration of mobile, buoyant CO_2 in a saline aquifer falls into a broad class of fluid-mechanics problems known as gravity currents, wherein a finite amount or known flux of one fluid is released or injected into a second, ambient fluid. Since the introduced fluid has a different density than the ambient fluid, the flow is governed by the balance of buoyancy and viscous dissipation.

Gravity currents have been well studied. Huppert (1982) investigated several cases of a fluid being released or injected into a less-dense and less-viscous ambient fluid on a flat surface for both planar and axisymmetric geometries (see references therein for earlier study on gravity currents). The relevant model for a gravity current in a porous medium has been known for quite some time: Bear (1972), for example, derives a sharp-interface model for the displacement of one fluid by another fluid of

different density and viscosity in a confined porous layer, including background flow, formation tilt and buoyant spreading (Bear 1972, p. 535, equation (9.5.64)).

Barenblatt, Entov & Ryzhik (1972) and Kochina, Mikhailov & Filinov (1983) studied the spreading of a mound of fluid surrounded by a less-dense and less-viscous ambient fluid in a porous medium, showing that the problem was asymptotically self-similar even when capillary trapping was included. Dussan V & Auzerais (1993) studied the buoyant spreading of fluid from a line source into a confined porous layer containing a denser ambient fluid. Huppert & Woods (1995) studied the buoyant spreading and along-slope migration of dense fluid in an unbounded porous layer.

More recently, Nordbotten, Celia & Bachu (2005) and Nordbotten & Celia (2006) studied the injection of CO_2 into a saline aquifer from a single well, giving a radially symmetric analytical solution for the case where injection-driven flow dominates buoyancy. Verdon & Woods (2007) considered a similar model in a different context, developing an analytical solution for injection in the planar geometry. Hesse, Tchelepi & Orr Jr (2006) studied the post-injection spreading and up-slope migration of a plume of CO_2, including capillary trapping as in Kochina *et al.* (1983). Hesse *et al.* (2007) studied the planar post-injection spreading of a plume of CO_2 and gave early- and late-time similarity solutions for buoyant spreading in a horizontal aquifer without capillary trapping, starting from a rectangular or 'step' initial shape. Hesse, Orr Jr & Tchelepi (2008) introduced capillary trapping to this model, showing that the early-time spreading behaviour remains self-similar when capillary trapping is included, and gave scaling results for the late-time spreading behaviour. Hesse *et al.* (2008) also considered the limit of up-slope migration with negligible spreading, starting from a step initial shape and including capillary trapping; they derived a semi-analytical solution in this limit, and an analytical solution for the case of negligible viscosity contrast.

Juanes & MacMinn (2008) and Juanes, MacMinn & Szulczewski (2010) considered CO_2 migration in a horizontal aquifer with a net groundwater through-flow, providing an explicit analytical solution for post-injection migration when buoyant spreading is negligible. Their solution included capillary trapping, as well as the reduced mobility of water in the region containing trapped CO_2, and also accounted for the tongued shape of the plume at the end of injection. This is important because capillary trapping causes the size of the plume at any time to depend strongly on the details of its evolution up to that time, and therefore the end-of-injection plume shape has a strong effect on the plume evolution for all time despite the diffusive mathematical character of the model (MacMinn & Juanes 2009).

Here, we study the post-injection migration of a CO_2 plume driven by groundwater flow in a tilted aquifer, including capillary trapping. As in Juanes & MacMinn (2008) and Juanes *et al.* (2010), we account for the tongued shape of the plume at the end of the injection period because this serves as the initial condition for post-injection migration. We confirm that the buoyant spreading term has a negligible effect on the long-time evolution of the plume (Juanes & MacMinn 2008; Hesse *et al.* 2008; Juanes *et al.* 2010), and we derive a complete analytical solution to the migration equation in the hyperbolic limit. We study the behaviour of the solution in different regions of the parameter space in terms of the storage efficiency, a macroscopic measure of plume migration related to the ultimate migration distance. In a future study we shall incorporate dissolution into the migration equation and study the importance of dissolution relative to capillary trapping, as well as the impact of dissolution on the storage efficiency. In Juanes *et al.* (2010) and Szulczewski & Juanes (2009) we show how these results can be used for basin-specific capacity estimation.

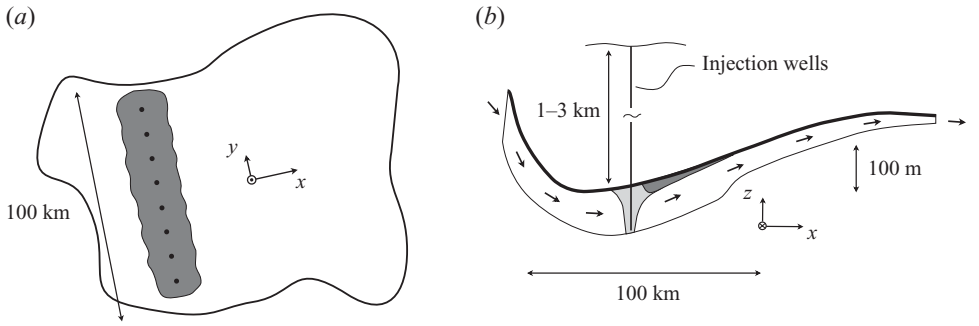

FIGURE 1. Injection of CO_2 into a saline aquifer at the basin scale. (*a*) From a bird's-eye view, the plumes from the individual wells merge together as the CO_2 spreads away from the well array (black dots). (*b*) In cross-section, the CO_2 is shown in grey, the groundwater in white, and the caprock as a thick line. Arrows indicate the direction of groundwater flow. Typical horizontal and vertical scales are indicated. Note that the vertical scale of the aquifer is greatly exaggerated.

2. Theoretical model for CO_2 migration

We are interested in large CO_2 storage projects, and therefore in the evolution of the CO_2 plume at the geologic basin scale; a schematic of the basin-scale geologic setting is shown in figure 1. We assume that the CO_2 is injected simultaneously through a linear arrangement of a large number of wells, known as a 'line drive' well array, as proposed by Nicot (2008). While the injection from a single well is radially outwards, the plumes from neighbouring wells will merge as the radius of the plumes approaches the inter-well spacing. We model the single resulting plume as two-dimensional in the x–z plane, with some width, W, in the y-direction equal to the length of the well array. While a two-dimensional model cannot capture three-dimensional flow effects such as groundwater or counter-current flow around the plume, or buoyant spreading in the lateral direction, the assumption of line symmetry is justified here when the well array is long relative to the typical extent of the CO_2 plume in the x-direction. Further, we are interested in scenarios where the volume of CO_2 injected is large, so that the typical extent of the plume in the x-direction is much larger than the thickness of the formation into which we inject.

We take the aquifer to be homogeneous, with an arbitrary tilt relative to the horizontal and a net groundwater through-flow to the right. We take the fluids to be incompressible and Newtonian, with constant and uniform properties within the aquifer. The fraction of pore space occupied by trapped or residual CO_2 after the bulk is displaced is the residual gas saturation, S_{gr}. Similarly, some fraction of pore space may be occupied by immobile groundwater; this is known as the connate water saturation, S_{wc}.

We employ a sharp-interface approximation, neglecting the width of typical gradients in saturation (i.e. the capillary transition zone or 'fringe') compared to typical length scales in the horizontal and vertical directions, and we further neglect the capillary pressure compared to typical hydrostatic and viscous pressure drops (see e.g. Bear 1972; Yortsos 1995).

In accordance with the sharp-interface approximation, we divide the domain into three regions of uniform CO_2 and groundwater saturation with sharp interfaces corresponding to saturation discontinuities. As illustrated in figure 2, region 1 is the mobile plume of CO_2, containing mobile CO_2 and a saturation S_{wc} of connate

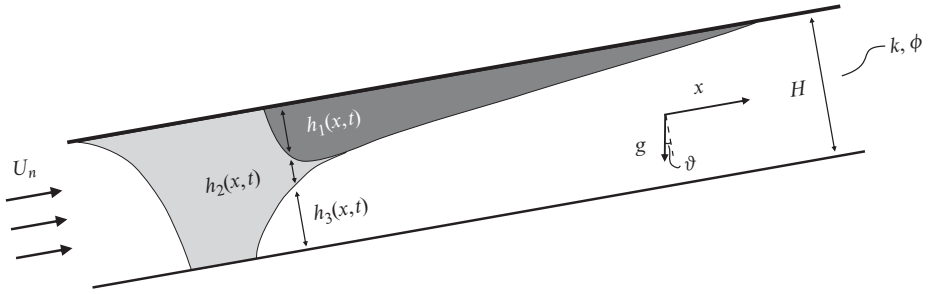

FIGURE 2. A schematic of the plume during post-injection migration, as the mobile CO_2 is pushed to the right by a combination of groundwater flow and aquifer slope, leaving trapped CO_2 in its wake. We divide the domain into three regions of uniform CO_2 and groundwater saturation, separated by sharp interfaces corresponding to saturation discontinuities. Region 1 (dark grey) has a saturation $1-S_{wc}$ of mobile CO_2 and a saturation S_{wc} of connate groundwater; region 2 (light grey) has a saturation S_{gr} of trapped CO_2 and a saturation $1-S_{gr}$ of mobile groundwater; region 3 (white) contains only groundwater. The aquifer has a total thickness H, and the thickness of region i, $i=1, 2, 3$, is denoted $h_i(x, t)$. Groundwater flows naturally through the aquifer from left to right with velocity U_n; the aquifer has permeability k and porosity ϕ, as well as an arbitrary angle of tilt, ϑ, measured anticlockwise from the direction of gravity.

groundwater; region 2 is the region from which the plume has receded, containing mobile groundwater and a saturation S_{gr} of trapped CO_2; and region 3 contains mobile groundwater and no CO_2.

We make the Dupuit or 'vertical equilibrium' approximation and neglect the vertical flow velocity compared to the horizontal flow velocity. This is justified when the characteristic vertical length scale is much smaller than the characteristic horizontal one (i.e. $H/L_c \ll 1$). This is generally the case for aquifers, which are typically very thin compared to their horizontal dimensions (see, again, Bear 1972; Yortsos 1995), and is further justified here by the fact that we consider scenarios where the volume of CO_2 injected is large, so that the typical extent of the plume in the x-direction is much larger than the thickness of the formation into which we inject.

With these assumptions, we can write the Darcy velocity for each phase in each region and relate them through conservation of mass, accounting carefully for the residual fluid that crosses each interface (Hesse *et al.* 2006, 2008). The resulting migration equation is

$$\widetilde{\mathscr{R}}\frac{\partial h_1}{\partial t}+\left[\frac{Q}{(1-S_{wc})\phi}\right]\frac{\partial f}{\partial x}+\kappa\sin\vartheta\,\frac{\partial}{\partial x}\left[(1-f)\,h_1\right] - \kappa\cos\vartheta\,\frac{\partial}{\partial x}\left[(1-f)\,h_1\,\frac{\partial h_1}{\partial x}\right]=0. \quad (2.1)$$

The discontinuous accumulation coefficient $\widetilde{\mathscr{R}}$ captures the volume loss due to capillary trapping by taking different values for drainage (h_1 increasing) and imbibition (h_1 decreasing),

$$\widetilde{\mathscr{R}}=\begin{cases}1, & \text{if} \quad \partial h_1/\partial t>0 \ \text{ and } \ h_2=0,\\ 1-\Gamma, & \text{otherwise.}\end{cases} \quad (2.2)$$

The parameter $\Gamma=S_{gr}/(1-S_{wc})$ is the capillary-trapping number, which measures the fraction of CO_2 that is left behind at the imbibition front and takes a constant

value between zero (no trapping) and one. A net volume rate Q of fluid flows through the aquifer from left to right. The nonlinear function $f(h_1, h_2, h_3)$ is given by

$$f(h_1, h_2, h_3) = \frac{\lambda_1 h_1}{\lambda_1 h_1 + \lambda_2 h_2 + \lambda_3 h_3}. \tag{2.3}$$

The thicknesses, h_i, are related through the requirement that they sum to the total aquifer thickness, $h_1 + h_2 + h_3 = H$, and through the relationship

$$\frac{\partial h_1}{\partial t} = \begin{cases} -\dfrac{\partial h_3}{\partial t}, & \text{if} \quad \partial h_1/\partial t > 0 \ \text{ and } \ h_2 = 0, \\ -\dfrac{\partial h_2}{\partial t}, & \text{otherwise}, \end{cases} \tag{2.4}$$

which reflects the difference between imbibition, when CO_2 is trapped, and drainage, when it is not. The characteristic velocity of buoyancy-driven flow in this system is

$$\kappa = \frac{\Delta\rho g k \lambda_1}{(1 - S_{wc})\phi}, \tag{2.5}$$

where $\Delta\rho = \rho_w - \rho_g$ is the density difference between the groundwater and the CO_2, g is the force per unit mass due to gravity and k and ϕ are the intrinsic permeability and porosity of the aquifer, respectively. We denote the mobility of the mobile phase in region i, $i = 1, 2, 3$, by $\lambda_i = k_{ri}/\mu_i$, where k_{ri} and μ_i are the relative permeability to that phase and the viscosity of that phase, respectively.

We expect the relative permeability to groundwater in region 2 to be less than that in region 3 because of the presence of the trapped gas there. In order to make analytical progress, however, we explicitly neglect this effect and assume that $\lambda_2 = \lambda_3$. This simplifies (2.1) substantially because the distinction between regions 2 and 3 no longer has physical significance, and the nonlinear function $f(h_1, h_2, h_3)$ can be rewritten as a function of h_1 only,

$$f(h_1) = \frac{\lambda_1 h_1}{\lambda_1 h_1 + \lambda_3 (H - h_1)}. \tag{2.6}$$

Note that Juanes & MacMinn (2008) solve (2.1) for $\vartheta = 0$ without making this approximation. With (2.6), (2.1) is of the same form as that presented in Bear (1972, p. 535, equation (9.5.64)) when $\Gamma = 0$ (no capillary trapping), and agrees with that of Hesse *et al.* (2008) when $Q = 0$ (no flow) and with that of Juanes *et al.* (2010) when $\vartheta = 0$ (no slope). We write (2.1) in dimensionless form,

$$\widetilde{\mathscr{R}} \frac{\partial \eta}{\partial \tau} + N_f \frac{\partial f}{\partial \xi} + N_s \frac{\partial}{\partial \xi}\left[(1 - f)\,\eta\right] - N_g \frac{\partial}{\partial \xi}\left[(1 - f)\,\eta \frac{\partial \eta}{\partial \xi}\right] = 0, \tag{2.7}$$

where $\eta = h_1/H$, $\tau = t/T_c$ and $\xi = x/L_c$, and with

$$\widetilde{\mathscr{R}} = \begin{cases} 1, & \text{if} \quad \partial\eta/\partial\tau > 0, \\ 1 - \Gamma, & \text{if} \quad \partial\eta/\partial\tau < 0, \end{cases} \tag{2.8}$$

and

$$f(\eta) = \frac{\mathscr{M}\eta}{\mathscr{M}\eta + (1 - \eta)}, \tag{2.9}$$

where $\mathscr{M} = \lambda_1/\lambda_3$ is the mobility ratio. We choose the characteristic length scale to be the length of a rectangle of aquifer of height H and containing a volume $Q_i T_i/2$ of CO_2, $L_c = Q_i T_i/2(1 - S_{wc})\phi H$, where Q_i is the volume rate of injection per unit length

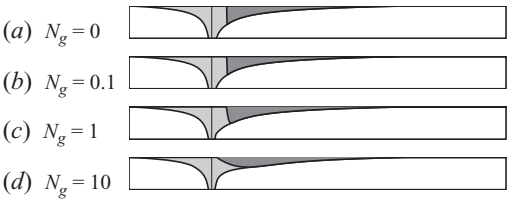

FIGURE 3. Numerical solutions to (2.7) for the shape of the plume during post-injection migration at $\tau = 2.25$ for $\mathscr{M} = 5$, $\Gamma = 0.3$, $N_f = 1$, $N_s = 0.5$ and $N_g = 0$, 0.1, 1 and 10. Qualitatively, plume migration – in particular, the prominent gravity tongue, the position of the leading edge, and the shape of the profile of trapped gas – is little affected by non-negligible values of N_g compared to N_f or N_s. In practice, the value of the mobility ratio $\mathscr{M}$ is larger (usually between 10 and 20), and the impact of the spreading term is even smaller.

of well array during the injection period and T_i is the duration of the injection period. The characteristic time scale T_c is arbitrary. The constants N_f, N_s and N_g are given by

$$N_f = \frac{T_c}{T_i}\frac{Q}{Q_i/2}, \quad N_s = \frac{T_c}{L_c}\kappa \sin\vartheta, \quad N_g = \frac{T_c}{L_c}\kappa \cos\vartheta \frac{H}{L_c}. \tag{2.10}$$

Without loss of generality, we choose $N_f \geqslant 0$: thus groundwater flow is always to the right by convention. Aquifer slope can be either positive ($N_s > 0$) for anticlockwise aquifer tilt or negative ($N_s < 0$) for clockwise aquifer tilt.

Equation (2.7) consists of a conditional accumulation term balanced by three nonlinear flux terms. The discontinuous nature of the accumulation term captures the effect of capillary trapping. The flux terms have the following physical interpretations: the first is advective in nature, capturing the motion of the CO_2 due to groundwater flow through the aquifer; the second is also advective, capturing the motion of the CO_2 due to the tilt of the aquifer; and the third is diffusive, capturing the upwards spreading of the CO_2 against the caprock due to buoyancy.

2.1. *Hyperbolic limit*

In order to simplify the solution of (2.7), we neglect the diffusive spreading term. This is justified because the essential features of the plume shape and migration are dominated by advective effects and capillary trapping, even for non-negligible values of N_g compared to N_f and N_s (Hesse *et al.* 2008; Juanes & MacMinn 2008; Juanes *et al.* 2010). This is illustrated qualitatively in figure 3, where we solve (2.7) numerically for several values of N_g.

Neglecting the spreading term, we rewrite (2.7) as

$$\frac{\partial \eta}{\partial \tau} + \frac{1}{\widetilde{\mathscr{R}}}\frac{\partial}{\partial \xi}F(\eta) = 0, \tag{2.11}$$

with flux function $F(\eta)$ given by

$$F(\eta) = N_f f + N_s(1-f)\eta. \tag{2.12}$$

Equation (2.11) is a first-order autonomous hyperbolic conservation law. We next solve it analytically, accounting for the shape of the plume at the end of injection. To aid in the derivation, we define a scaled and shifted plume thickness $g(\xi, \tau)$,

$$g = (\mathscr{M} - 1)\eta + 1, \tag{2.13}$$

that re-maps plume thicknesses $0 \leqslant \eta \leqslant 1$ to $1 \leqslant g \leqslant \mathscr{M}$. We also define a corresponding flux function G,

$$G(g) = (\mathscr{M} - 1)F, \tag{2.14}$$

so that we can rewrite (2.11),

$$\frac{\partial g}{\partial \tau} + \frac{1}{\widetilde{\mathscr{R}}}\frac{\partial}{\partial \xi}G(g) = 0. \tag{2.15}$$

The solution to this equation depends on three dimensionless parameters: $\mathscr{M}$, Γ and the ratio N_s/N_f.

2.2. *The injection period*

The solution of (2.15) for the injection period has been discussed by Nordbotten *et al.* (2005) and Nordbotten & Celia (2006) for the radial geometry and, in a different context, by Verdon & Woods (2007) for the planar geometry. Here, we re-derive the latter in the context of CO_2 injection. During injection, we assume that a constant volume rate, Q_i, of CO_2 per unit length of the line-drive well array is pumped into the aquifer. Injection typically dominates the flow, and we therefore neglect natural groundwater flow and slope relative to injection, $Q_i \gg U_n H$ and $N_s/N_f \ll 1$. We then assume that the flow rate Q_i is split evenly between the left and right sides of the injection well, and therefore that the plume shape is symmetric across the injection well. Groundwater flow and aquifer slope would lead to some asymmetry in the plume shape, but we expect this to be negligible due to the dominance of injection.

Considering now the right-hand side of the well only, we model the well as a line source located at $\xi = 0$ and with strength $Q_i/2H$ per unit vertical length. We take the characteristic time scale to be the duration of injection so that $\tau = 1$ is the end of the injection period and $N_f = 1$.

The solution to a hyperbolic conservation law such as (2.15) is a collection of waves travelling through space–time at constant speed. These waves behave independently of one another unless they collide. The speed of each wave is determined by its thickness, g, and is given by $G'(g)/\widetilde{R}$ where $G' = \mathrm{d}G/\mathrm{d}g$. The flux function, $G(g)$, for the right front during injection is concave down and strictly increasing, so the right front evolves as a 'rarefaction': all waves travel to the right and the front is stretched horizontally. Because all waves correspond to CO_2 displacing groundwater to the right, all waves are in drainage with $\widetilde{\mathscr{R}} = 1$.

The plume shape is symmetric across the injection well because we have neglected groundwater flow and slope relative to injection, so the left front, ξ_L, is simply the reflection of the right front, ξ_R,

$$\xi_L(g,\tau) = -\left(\frac{\mathscr{M}}{g^2}\right)\tau, \quad \xi_R(g,\tau) = \left(\frac{\mathscr{M}}{g^2}\right)\tau. \tag{2.16}$$

Figure 4 shows the characteristics and the plume shape at several times during the injection period, which ends at $\tau = 1$. The shape of the plume at the end of the injection period serves as the initial condition for post-injection migration (Juanes & MacMinn 2008; MacMinn & Juanes 2009; Juanes *et al.* 2010).

3. Post-injection migration

Once injection has ended, the plume migrates due to both slope and groundwater flow, and is subject to residual trapping. We solve (2.15) for post-injection migration using the method of characteristics. The post-injection problem is more difficult than the injection problem because of the complex interactions between slope, groundwater flow and capillary trapping: waves collide, and we divide the analysis into parts based on the types of collisions that occur.

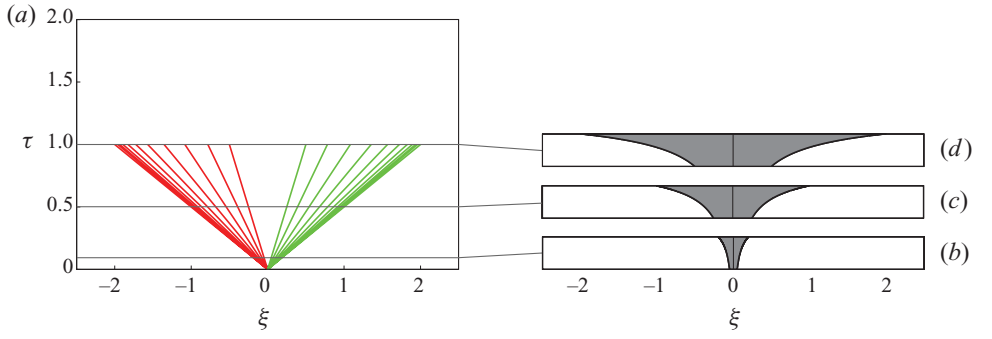

FIGURE 4. (Colour online) During injection with $\mathscr{M} = 2$, (*a*) the evolution of the plume in characteristic space and (*b*)–(*d*) the shape of the plume (grey) at $\tau = 0.1$, 0.5 and 1, respectively. In (*a*), we show several waves of the left and right fronts in red and green, respectively; the innermost and outermost waves on each front correspond to $g = \mathscr{M}$ and $g = 1$ ($\eta = 1$ and $\eta = 0$), respectively.

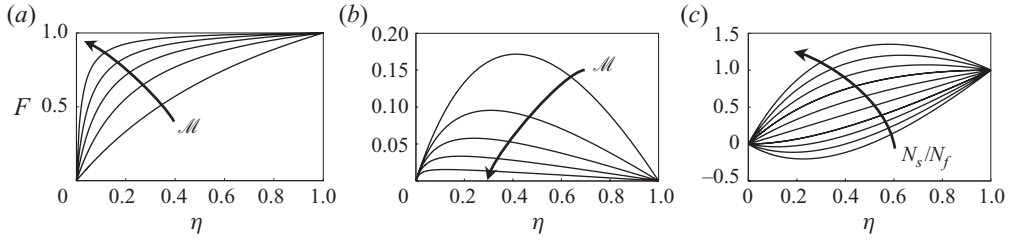

FIGURE 5. The shape of the flux function for (*a*) flow only ($N_s = 0$, $N_f = 1$) for $M = 2$, 5, 10, 20 and 50; (*b*) positive slope only ($N_s = 1$, $N_f = 0$) for $M = 2$, 5, 10, 20 and 50 and (*c*) combined flow and slope for $M = 2$, $N_f = 1$ and N_s varying from -4 to 4.

The characteristic time scale in post-injection is arbitrary, but in order to maintain a continuous time variable we redefine τ in post-injection as

$$\tau = 1 + \frac{t - T_i}{T_c}, \tag{3.1}$$

so that the end of injection, $t = T_i$, always corresponds to $\tau = 1$.

As during injection, the velocity of each wave of the left and right fronts is given by the corresponding derivative of the flux function, $G'(g)$, scaled by $\widetilde{\mathscr{R}}$. The direction in which each wave travels (i.e. to the left or to the right) is determined by the sign of $G'(g)$, and this in turn sets the appropriate value of $\widetilde{\mathscr{R}}$ for each wave: waves of the left front moving to the left correspond to CO_2-displacing groundwater, and are then drainage waves; waves of the left front moving to the right correspond to groundwater displacing CO_2, and are imbibition waves. Waves of the right front moving to the left or to the right are similarly imbibition waves or drainage waves, respectively.

We plot the flux functions for flow only, for slope only, and for combined flow and slope in figure 5. The flux function for flow only is concave down and strictly increasing – in other words, we say that flow pushes all waves to the right. In contrast, the flux function for positive slope only is concave down with a local maximum at some $\eta = \eta_s$: waves with $\eta < \eta_s$ move up-slope, the wave with $\eta = \eta_s$ is stationary and waves with $\eta > \eta_s$ move down-slope (Hesse *et al.* 2008). The flux function for negative

slope has the opposite behaviour. We take the three limiting cases of negative slope only, flow only, and positive slope only to be three discrete points on the continuum of possible values of the parameter N_s/N_f: these are $N_s/N_f \to -\infty$, $N_s/N_f = 0$ and $N_s/N_f \to \infty$, respectively. To understand qualitatively the effect of combined flow and slope, consider a flow-only system where all waves move to the right. Adding some amount of positive slope will 'speed' the upper portion of the plume and 'slow' the lower portion; if the amount of positive slope is large enough, a stationary point will be introduced at some $\eta = \eta_s$ and waves with $\eta > \eta_s$ will move to the left. Adding negative slope to a flow-only system will accomplish the opposite, slowing the upper portion of the plume and speeding the lower portion; if the amount of negative slope is large enough, a stationary point will be introduced at some $\eta = \eta_s$ and waves with $\eta < \eta_s$ will move to the left.

To understand this behaviour quantitatively, consider the derivative of the flux function,

$$G' = \frac{\mathrm{d}G}{\mathrm{d}g} = -\left[\left(\frac{1}{\mathscr{M}-1}\right)N_s\right] + \left[\mathscr{M}N_f + \left(\frac{\mathscr{M}}{\mathscr{M}-1}\right)N_s\right]\frac{1}{g^2}, \tag{3.2}$$

which changes sign once at stationary point $g = g_s$ given by

$$g_s = \sqrt{\mathscr{M}(\mathscr{M}-1)N_f/N_s + \mathscr{M}}. \tag{3.3}$$

From (3.3), g_s exists on the interval $1 \leqslant g \leqslant \mathscr{M}$ only for $N_s/N_f \leqslant -\mathscr{M}$ or $1 \leqslant N_s/N_f$. Accordingly, the continuum of possible values of the ratio N_s/N_f can be divided into three intervals based on the nature of the resulting plume migration. For $N_s/N_f \leqslant -\mathscr{M}$, the flux function is concave up and has a local minimum, so that G' vanishes at $g = g_s$ and is negative for $g < g_s$ and positive for $g > g_s$: we refer to this interval as 'negative slope with weak flow'. For $-\mathscr{M} < N_s/N_f < 1$, the flux function is concave up for $N_s/N_f < -(\mathscr{M}-1)$, linear for $N_s/N_f = -(\mathscr{M}-1)$ and concave down for $N_s/N_f > -(\mathscr{M}-1)$, and in all cases strictly increasing so that G' is positive: we refer to this interval as 'flow with weak slope'. For $1 \leqslant N_s/N_f$, the flux function is concave down and has a local maximum, so that G' vanishes at $g = g_s$ and is positive for $g < g_s$ and negative for $g > g_s$: we refer to this interval as 'positive slope with weak flow'. The flux functions and the resulting plume motion for these three intervals are illustrated in figure 6.

3.1. *Flow with weak slope*

We consider $-\mathscr{M} < N_s/N_f < 1$, for which G' is strictly positive. Starting from the end-of-injection shape, all waves propagate to the right at speed $G'(g)/\widetilde{R}$ until two or more waves collide. The right front is a drainage front with $\widetilde{\mathscr{R}} = 1$ and the left front is an imbibition front with $\widetilde{\mathscr{R}} = (1 - \Gamma)$. Because of this, a given wave on the left front travels faster than the corresponding wave on the right front.

As the plume migrates, one of the two fronts will be compacted and the other will be stretched. If the flux function is concave up ($N_s/N_f < -(\mathscr{M}-1)$), waves for larger values of g will travel faster than waves for smaller values and the left front will be stretched as the right front is compacted; if the flux function is concave down ($N_s/N_f > -(\mathscr{M}-1)$), waves for larger values of g will travel more slowly than waves for smaller values and the left front will be compacted as the right front is stretched. In the particular case when the flux function is a straight line ($N_s/N_f = -(\mathscr{M}-1)$), all waves on each front move at the same speed and the fronts will not change shape as they travel.

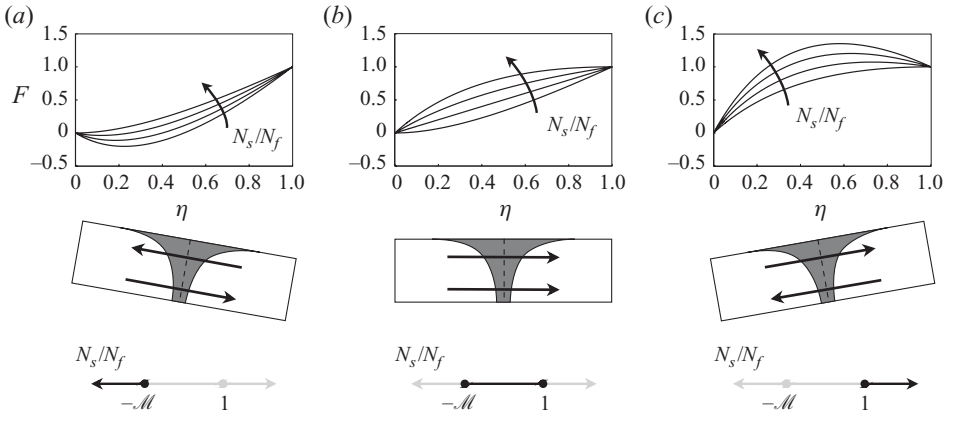

FIGURE 6. The shape of the flux function and the resulting plume motion for (a) negative slope with weak flow, (b) flow with weak slope and (c) positive slope with weak flow for $M = 2$. The direction of N_s/N_f increasing is indicated. Note that the curvature of the flux function changes sign at $N_s/N_f = -(\mathscr{M} - 1)$ in the flow-with-weak-slope interval.

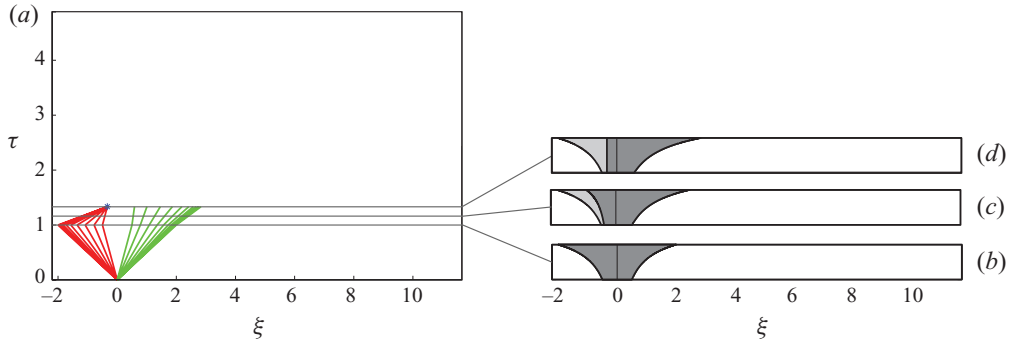

FIGURE 7. (Colour online) A shock forms when a portion of a front is compressed into a discontinuity. Here ($\mathscr{M} = 2$, $\Gamma = 0.5$, $N_f = 1$, $N_s = 0.5$), the entire left front becomes a shock as (a) the characteristics collide at a single point. The shapes of the plume at (b) the end of injection, (c) an intermediate time and (d) the time of shock formation are also shown.

It is possible that the compacting front will eventually become a discontinuity or 'shock'. Shocks are a common feature of nonlinear hyperbolic conservation laws. The formation of a shock corresponds to multiple waves meeting at a single point and thereafter travelling together through space–time. The formation of a shock is illustrated in figure 7. It is also possible that a wave from the left front will catch the corresponding wave from the right front, meaning that all of the CO_2 in between has been trapped. When this occurs, we refer to the point of intersection of the left and right fronts as a 'peak'. The formation of a peak is illustrated in figure 8. Peak formation is unusual in that the collision of two waves at a peak corresponds to the end of those characteristics in space–time: those two waves cease to exist. Peak formation is possible here because capillary trapping causes imbibition waves to travel faster than drainage waves.

The formation of a shock or peak leads to a fundamental change in the migration behaviour, so we must determine when and where these collisions occur. To do so, we

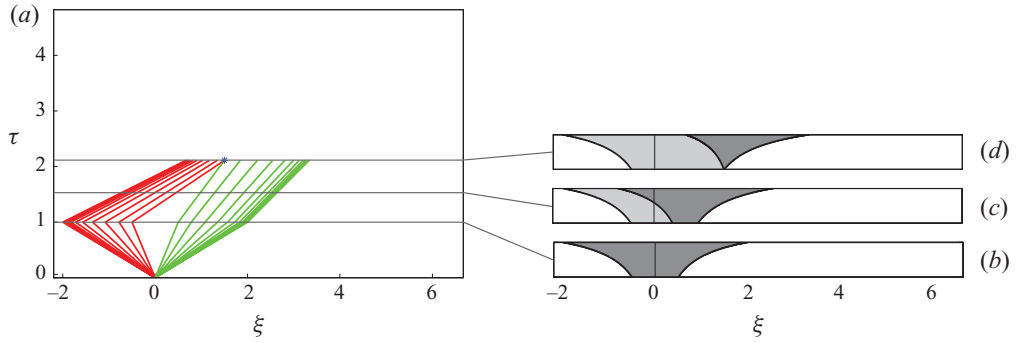

FIGURE 8. (Colour online) A peak forms when the left and right fronts touch, i.e. when all of the CO_2 between is trapped. Here ($\mathscr{M} = 2$, $\Gamma = 0.5$, $N_f = 1$, $N_s = -0.8$), a peak forms at the bottom of the plume as (*a*) the two innermost characteristics collide. The shapes of the plume at (*b*) the end of injection, (*c*) an intermediate time and (*d*) the time of peak formation are also shown.

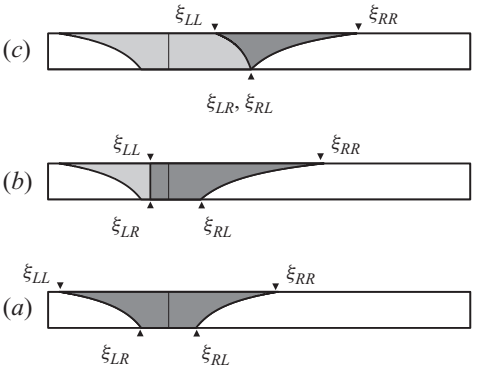

FIGURE 9. In order to determine when and where collisions occur, we examine (*a*) the positions of four key points: ξ_{LL} and ξ_{LR} are the left-most and right-most points, respectively, on the left front, and ξ_{RL} and ξ_{RR} are the left-most and right-most points on the right front. The mobile CO_2 is shown in dark grey, the region with trapped gas in light grey. We can see that (*b*) a shock forms on the left when point ξ_{LL} collides with point ξ_{RR}, or that a peak forms (*c*) when point ξ_{LR} collides with point ξ_{RL}. It is also possible for a shock to form on the right when point ξ_{RL} collides with point ξ_{RR} (see the discussion of cases 4 and 5 in §§ 3.1.4 and 3.1.5).

examine the positions of four key points: these are here the left-most and right-most points on each front, as shown in figure 9. A shock or peak will form when any two key points collide. The positions of these key points are

$$\xi_{LL}(\tau) = -\mathscr{M} + \frac{1}{1-\Gamma}(\mathscr{M}N_f + N_s)(\tau - 1), \tag{3.4a}$$

$$\xi_{LR}(\tau) = -\frac{1}{\mathscr{M}} + \frac{1}{1-\Gamma}\left(\frac{N_f - N_s}{\mathscr{M}}\right)(\tau - 1), \tag{3.4b}$$

$$\xi_{RL}(\tau) = \frac{1}{\mathscr{M}} + \left(\frac{N_f - N_s}{\mathscr{M}}\right)(\tau - 1), \tag{3.4c}$$

$$\xi_{RR}(\tau) = \mathscr{M} + (\mathscr{M}N_f + N_s)(\tau - 1), \tag{3.4d}$$

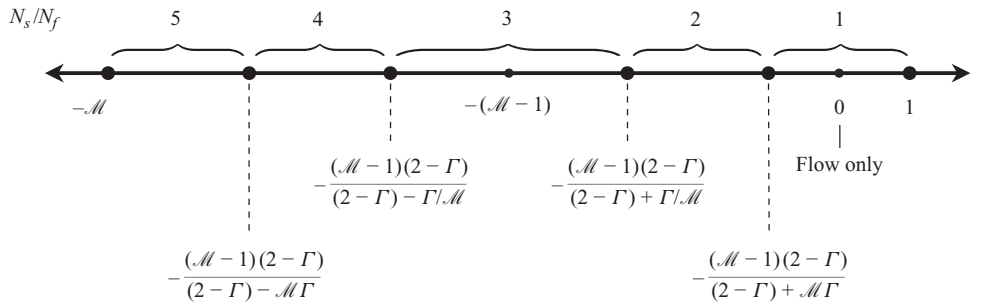

FIGURE 10. We divide the flow-with-weak-slope interval into five cases by comparing the collision times from (3.5) with one another. Note that case 5 exists only if $\mathscr{M} < \sqrt{2/\Gamma - 1}$, which is typically not the case; otherwise, case 4 extends to $-\mathscr{M}$. The case of flow only studied by Juanes & MacMinn (2008) and Juanes *et al.* (2010) is within case 1.

where ξ_{LL} and ξ_{LR} are the left-most and right-most points, respectively, on the left front and ξ_{RL} and ξ_{RR} are the left-most and right-most points on the right front. These expressions remain valid until the first collision occurs.

We use the notation $\xi_{\alpha\beta} \to \xi_{\gamma\delta}$ to indicate the collision of the former key point with the latter. Because all points move to the right in this interval, it is clear that the first collision must be one of $\xi_{LL} \to \xi_{LR}$, $\xi_{LR} \to \xi_{RL}$ or $\xi_{RL} \to \xi_{RR}$. The times at which these three collisions would occur are readily derived from (3.4):

$$\tau_{LL}^{LR} = 1 + \frac{(1-\Gamma)(\mathscr{M}-1)}{(\mathscr{M}-1)N_f + N_s}, \tag{3.5a}$$

$$\tau_{LR}^{RL} = 1 + \frac{2(1-\Gamma)}{\Gamma(N_f - N_s)}, \tag{3.5b}$$

$$\tau_{RL}^{RR} = 1 - \frac{(\mathscr{M}-1)}{(\mathscr{M}-1)N_f + N_s}, \tag{3.5c}$$

where $\tau_{\alpha\beta}^{\gamma\delta}$ is the time corresponding to $\xi_{\alpha\beta} \to \xi_{\gamma\delta}$. By comparing these collision times with one another, we can divide the flow-with-weak-slope interval, $-\mathscr{M} < N_s/N_f < 1$, into five cases based on the order in which collisions occur, as illustrated in figure 10.

3.1.1. *Case 1*

The development of case 1 is a simple generalization of the flow-only case. The flux function is concave down, so the left front is compacted while the right front is stretched. The first collision is $\xi_{LL} \to \xi_{LR}$, which occurs at position

$$\xi_{LL}^{LR} = \frac{-N_s/N_f}{(\mathscr{M}-1) + N_s/N_f} \tag{3.6}$$

and at time τ_{LL}^{LR} from (3.5). When this occurs, the entire left front becomes a shock that propagates to the right at a constant speed until it collides with ξ_{RL}. The speed of the shock, σ, during this period is evaluated from the Rankine–Hugoniot condition (see e.g. Lax 1972),

$$\sigma = \frac{1}{1-\Gamma}\frac{[\![G]\!]}{[\![g]\!]} = \frac{N_f}{1-\Gamma}, \tag{3.7}$$

where the notation $[\![\circ]\!]$ indicates the difference or 'jump' in the indicated quantity across the shock. The shock collides with ξ_{RL} at position

$$\xi_\sigma^{RL} = \frac{(2-\Gamma)-(1-\Gamma)N_s/N_f}{(\mathscr{M}-(1-\Gamma))+(1-\Gamma)N_s/N_f} \tag{3.8}$$

and time

$$\tau_\sigma^{RL} = 1 + \frac{(1-\Gamma)(\mathscr{M}+1)}{(\mathscr{M}-(1-\Gamma))N_f+(1-\Gamma)N_s}. \tag{3.9}$$

Thereafter, the shock collides continuously with the right front. We develop a differential equation for the shock height by posing the collision of the shock with an arbitrary wave g^* on the right front at some time τ^*. The position of the shock at time τ^* can be written

$$\xi_\sigma(\tau^*) = \xi_\sigma^{RL} + \int_{\tau_\sigma^{RL}}^{\tau^*} \sigma(\tau)\,\mathrm{d}\tau, \tag{3.10}$$

where the shock speed at any time is evaluated from the Rankine–Hugoniot condition for the instantaneous shock height. The position of the wave g^* on the right front prior to collision with the shock can be written

$$\xi_{g^*}(\tau^*) = \frac{\mathscr{M}}{g^{*2}} + G'(g^*)(\tau^*-1). \tag{3.11}$$

Equating $\xi_\sigma(\tau^*)$ with $\xi_{g^*}(\tau^*)$, since these must be equal by the definition of τ^* and g^*, we differentiate the resulting expression with respect to τ^* and re-arrange to find the ordinary differential equation (ODE) for the shock height as a function of time,

$$\frac{\mathrm{d}g^*}{\mathrm{d}\tau^*} = \frac{\sigma(g^*)-G'(g^*)}{-2\mathscr{M}/g^{*3}+G''(g^*)(\tau^*-1)}. \tag{3.12}$$

Equation (3.12) is separable,

$$\int_{\mathscr{M}}^{g_\sigma} \frac{-2\mathscr{M}}{\sigma(g^*)+G'(g^*)}\frac{\mathrm{d}g^*}{g^{*3}} = \int_{\tau_\sigma^{RL}}^{\tau} \frac{\mathrm{d}\tau^*}{(N_f+N_s/(\mathscr{M}-1))(\tau^*-1)+1}, \tag{3.13}$$

where g_σ is the height of the shock at time τ, and has implicit solution

$$\mathscr{I}(g_\sigma)-\mathscr{I}(\mathscr{M}) = \ln\left[\frac{(N_f+N_s/(\mathscr{M}-1))(\tau-1)+1}{(N_f+N_s/(\mathscr{M}-1))\left(\tau_\sigma^{RL}-1\right)+1}\right] \tag{3.14}$$

where the integral $\mathscr{I}(g)$ is given by

$$\mathscr{I}(g) = \ln\left[\frac{(1-\Gamma)g^2}{(1-\Gamma)-g+B\Gamma g^2}\right] + 2A\,\mathrm{atan}\left[A(2B\Gamma g-1)\right], \tag{3.15}$$

with constants A and B,

$$A = \frac{1}{\sqrt{4B\Gamma(1-\Gamma)-1}}, \quad B = \frac{N_s/N_f}{\mathscr{M}(\mathscr{M}-1)+\mathscr{M}N_s/N_f}. \tag{3.16}$$

We now have an implicit analytical relationship for the shock height as a function of time, and the plume evolves accordingly until $g_\sigma \to 1$ when the shock catches ξ_{RR}, at which point the plume vanishes. The complete evolution of the plume for case 1 is shown in figure 11.

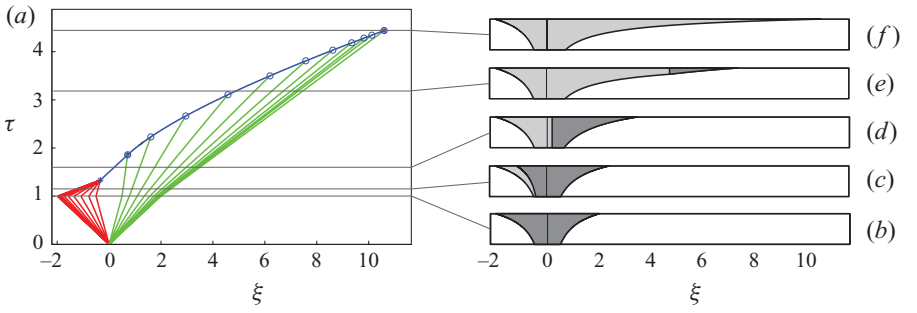

FIGURE 11. (Colour online) Post-injection migration for case 1 with $\mathscr{M} = 2$, $\Gamma = 0.5$, $N_f = 1$ and $N_s = 0.5$: (*a*) the evolution of the plume in characteristic space with waves of the left and right fronts in red and green, respectively, and the shock path in blue; (*b*)–(*f*) the shape of the plume at several times during migration, with mobile CO_2 in dark grey, the region containing trapped CO_2 in light grey and groundwater in white.

3.1.2. *Case 2*

In case 2, the flux function remains concave down so that the left front is again compacted as the right front is stretched, but $\xi_{LR} \to \xi_{RL}$ now occurs before $\xi_{LL} \to \xi_{LR}$ and a peak forms. This occurs at position

$$\xi_{LR}^{RL} = \frac{1}{\mathscr{M}}\left(\frac{2}{\Gamma} - 1\right) \tag{3.17}$$

and time

$$\tau_{LR}^{RL} = 1 + \frac{2(1-\Gamma)}{\Gamma(N_f - N_s)}. \tag{3.18}$$

The height of the peak g_p as a function of time is simply the height at which the left and right fronts intersect,

$$g_p = \sqrt{\mathscr{M}\left[(\mathscr{M}-1)N_f/N_s + 1\right] - \frac{2\mathscr{M}(\mathscr{M}-1)(1-\Gamma)}{\Gamma N_s(\tau - 1)}}. \tag{3.19}$$

The left and right fronts, meeting at the peak, then continue to compact and stretch, respectively, until the left front compacts into a shock, which occurs at position $\xi_p^{LR} = \xi_{LL}^{LR}$ from (3.4) and time $\tau_p^{LR} = \tau_{LL}^{LR}$ from (3.5). The height of the peak when this occurs is

$$g_p^{LR} = \sqrt{\mathscr{M}\left[(\mathscr{M}-1)N_f/N_s + 1\right]\left(1 - \frac{2}{\Gamma}\right)}. \tag{3.20}$$

This shock then travels to the right, colliding continuously with the right front until the plume vanishes. The evolution of the shock during this final period is analogous to the final period of evolution from case 1, but beginning at a different position and time, and with a different initial shock height. The complete evolution of the plume for case 2 is shown in figure 12.

3.1.3. *Case 3*

In case 3, the first collision is $\xi_{LR} \to \xi_{RL}$, forming a peak, and the second is ξ_{LL}^{RR}, at which point the plume is completely trapped. This occurs before either front is compressed into a shock; as a result, the expressions for the position and time at

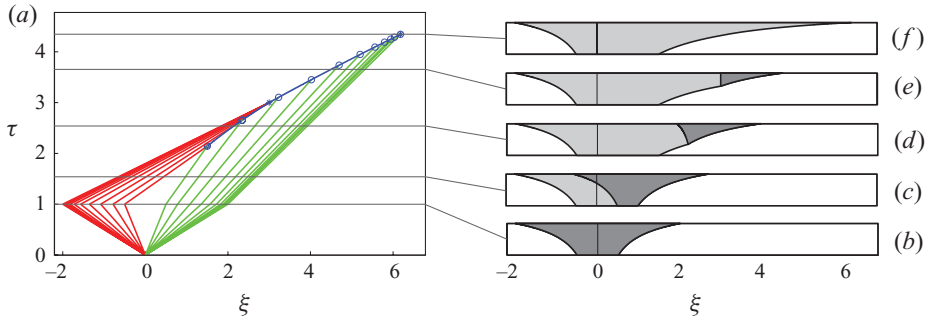

FIGURE 12. (Colour online) Post-injection migration for case 2 with $\mathscr{M} = 2$, $\Gamma = 0.5$, $N_f = 1$ and $N_s = -0.75$: (*a*) the evolution of the plume in characteristic space with waves of the left and right fronts in red and green, respectively, and the peak and shock paths in blue; (*b*)–(*f*) the shape of the plume at several times during migration, with mobile CO_2 in dark grey, the region containing trapped CO_2 in light grey and groundwater in white.

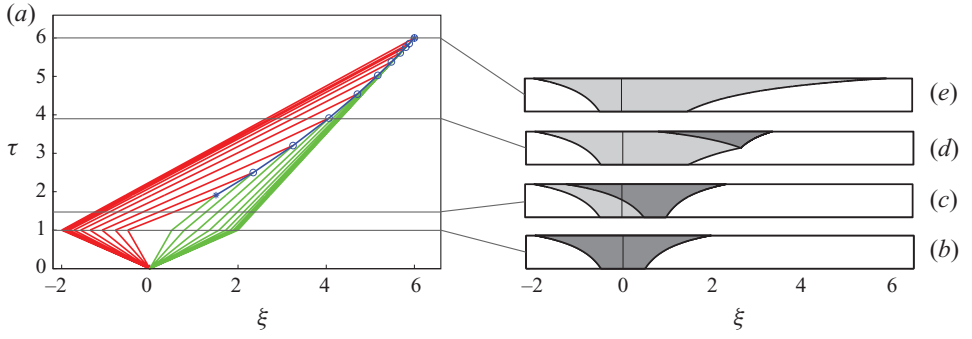

FIGURE 13. (Colour online) Post-injection migration for case 3 with $\mathscr{M} = 2$, $\Gamma = 0.5$, $N_f = 1$ and $N_s = -1.2$: (*a*) the evolution of the plume in characteristic space with waves of the left and right fronts in red and green, respectively, and the peak path in blue; (*b*)–(*e*) the shape of the plume at several times during migration, with mobile CO_2 in dark grey, the region containing trapped CO_2 in light grey and groundwater in white.

which the plume vanishes are particularly simple, and are given by

$$\xi_{LL}^{RR} = \mathscr{M}\left(\frac{2}{\Gamma} - 1\right) \tag{3.21}$$

and

$$\tau_{LL}^{RR} = 1 + \frac{2\mathscr{M}(1-\Gamma)}{\Gamma(\mathscr{M}N_f + N_s)}, \tag{3.22}$$

respectively. The complete evolution of the plume for case 3 is shown in figure 13. Note that the curvature of the flux function changes sign at $N_s/N_f = -(\mathscr{M} - 1)$, for which value the flux function is a straight line – this is always within case 3.

3.1.4. *Case 4*

In case 4, the flux function is now concave up and the left front is stretched, while the right front is compacted – in other words, we now expect shocks to form on the right. The first collision is again $\xi_{LR} \to \xi_{RL}$, forming a peak. The second collision is $\xi_p \to \xi_{RR}$, at which point the right front has been compacted into a shock. The shock

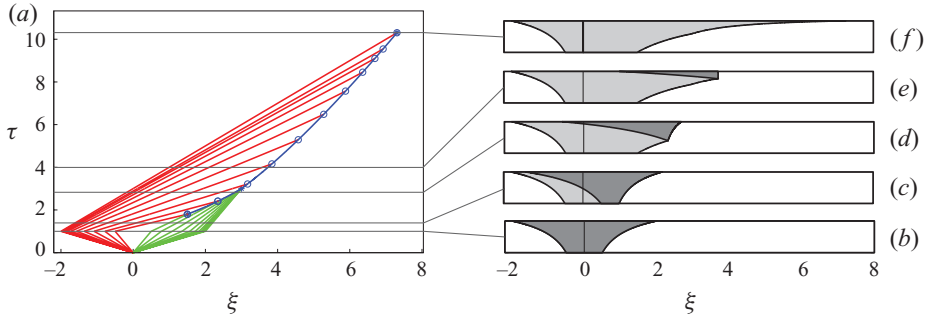

FIGURE 14. (Colour online) Post-injection migration for case 4 with $\mathscr{M} = 2$, $\Gamma = 0.5$, $N_f = 1$ and $N_s = -1.5$: (*a*) the evolution of the plume in characteristic space with waves of the left and right fronts in red and green, respectively, and the peak and shock paths in blue; (*b*)–(*f*) the shape of the plume at several times during migration, with mobile CO_2 in dark grey, the region containing trapped CO_2 in light grey and groundwater in white.

then propagates slowly to the right, colliding continuously with the left front as the latter overtakes it. The ODE for the shock height as a function of time differs only slightly from that of case 1: the construction is analogous and the result can again be integrated analytically. The complete evolution of the plume for case 4 is shown in figure 14.

3.1.5. *Case 5*

In case 5, the flux function remains concave up and the first collision is $\xi_{RL} \to \xi_{RR}$ as the right front is compacted into a shock. The shock then evolves in the same manner as in case 4 until the plume is completely trapped. This case exists only if $\mathscr{M} < \sqrt{2/\Gamma - 1}$, which is generally not the case for typical values of $\mathscr{M}$ and Γ for the CO_2 problem, and otherwise case 4 extends to $N_s/N_f = -\mathscr{M}$. Note that for the particular case of $N_s/N_f = -\mathscr{M}$ the speed of the points ξ_{LL} and ξ_{RR} is exactly 0; the plume thins as the shock travels slowly to the right, but the shock height approaches zero asymptotically and the plume never becomes fully trapped, although in reality it would be arrested by capillarity as it becomes very thin.

3.2. *Negative slope with weak flow*

When $N_s/N_f \leqslant -\mathscr{M}$, the flux function is concave up and has a local minimum at some $g = g_s$. The wave on each front corresponding to $g = g_s$ is stationary and does not move from its end-of-injection position; we must introduce these as two additional key points,

$$\xi_{LS}(\tau) = \frac{-1}{(\mathscr{M}-1)N_f/N_s + 1}, \tag{3.23a}$$

$$\xi_{RS}(\tau) = \frac{1}{(\mathscr{M}-1)N_f/N_s + 1}, \tag{3.23b}$$

where ξ_{LS} and ξ_{RS} are the stationary points on the left and right fronts, respectively. Waves corresponding to $g < g_s$ travel to the left and those corresponding to $g > g_s$ travel to the right; i.e. the 'upper' portion of the plume travels up-slope, against the flow, and the 'lower' portion of the plume travels down-slope, with the flow. As in cases 4 and 5, the left front will be stretched while the right front is compacted. Note

that unlike all of the previous cases, the net motion of the plume in this interval is now to the left, or up-slope.

The positions of the other four key points are

$$\xi_{LL}(\tau) = -\mathscr{M} + (\mathscr{M}N_f + N_s)(\tau - 1), \tag{3.24a}$$

$$\xi_{LR}(\tau) = -\frac{1}{\mathscr{M}} + \frac{1}{1-\Gamma}\left(\frac{N_f - N_s}{\mathscr{M}}\right)(\tau - 1), \tag{3.24b}$$

$$\xi_{RL}(\tau) = \frac{1}{\mathscr{M}} + \left(\frac{N_f - N_s}{\mathscr{M}}\right)(\tau - 1), \tag{3.24c}$$

$$\xi_{RR}(\tau) = \mathscr{M} + \frac{1}{1-\Gamma}(\mathscr{M}N_f + N_s)(\tau - 1). \tag{3.24d}$$

The first collision in this interval must be one of three possibilities: $\xi_{RR} \to \xi_{RS}$, $\xi_{RL} \to \xi_{RS}$ or $\xi_{LR} \to \xi_{RL}$. Ultimately, a shock must form at ξ_{RS} because it is stationary: this can either happen as the first collision ($\xi_{RR} \to \xi_{RS}$ or $\xi_{RL} \to \xi_{RS}$) or, if $\xi_{LR} \to \xi_{RL}$ occurs first, as the second. Once the shock forms, it must eventually collide with the peak if one has formed, or with ξ_{RL} and then with ξ_{LR} if one has not. It must then collide with ξ_{LS} and ultimately with ξ_{LL}. The shock may change direction during its evolution, switching from drainage to imbibition or *vice versa*, but this is at all times consistent with the Rankine–Hugoniot condition.

In the flow-with-weak-slope interval, the formation of the shock (if a shock forms) is always the last collision. This allowed us to examine the behaviour preceding the shock formation in great detail, and to divide the interval into cases accordingly. In the negative-slope-with-weak-flow interval, the formation of the shock is always one of the first two collisions and it is no longer tractable to determine the order of collisions in an explicit fashion. Instead, we implement a decision-tree algorithm to handle each stage of the plume evolution in sequence. The algorithm evaluates and compares the times at which possible collisions would occur, and evolves the plume accordingly: this process is entirely algebraic, consisting only of the evaluation of complex and sometimes implicit expressions.

We illustrate one example of the evolution of the plume in this interval in figure 15; the order of collisions in this example is $\xi_{RR} \to \xi_{RS}$ forming a shock, $\xi_{RL} \to \xi_\sigma$, $\xi_{LR} \to \xi_\sigma$, $\xi_\sigma \to \xi_{LS}$ and $\xi_\sigma \to \xi_{LL}$.

3.3. *Positive slope with weak flow*

When $1 \leqslant N_s/N_f$, the flux function is concave down and has a local maximum at some $g = g_s$. The waves corresponding to $g = g_s$ are again stationary, and we again have three key points on each front. Waves corresponding to $g < g_s$ now travel to the right and those corresponding to $g > g_s$ travel to the left; i.e.the upper portion of the plume travels up-slope, with the flow, and the lower portion of the plume travels down-slope, against the flow. As in cases 1 and 2 of the flow-with-weak-slope interval, the left front will be compacted, while the right front is stretched. Additionally, the net motion of the plume is again to the right.

The evolution of the plume is analogous to that in the negative-slope-with-weak flow interval: the first collision must be one of three possibilities: $\xi_{LL} \to \xi_{LS}$, $\xi_{LR} \to \xi_{LS}$ or $\xi_{RL} \to \xi_{LR}$. Ultimately, a shock must form at ξ_{LS} because it is stationary: this can either happen as the first collision ($\xi_{LL} \to \xi_{LS}$ or $\xi_{LR} \to \xi_{LS}$) or, if $\xi_{RL} \to \xi_{LR}$ occurs first, as the second. Once the shock forms, it must eventually collide with the peak if

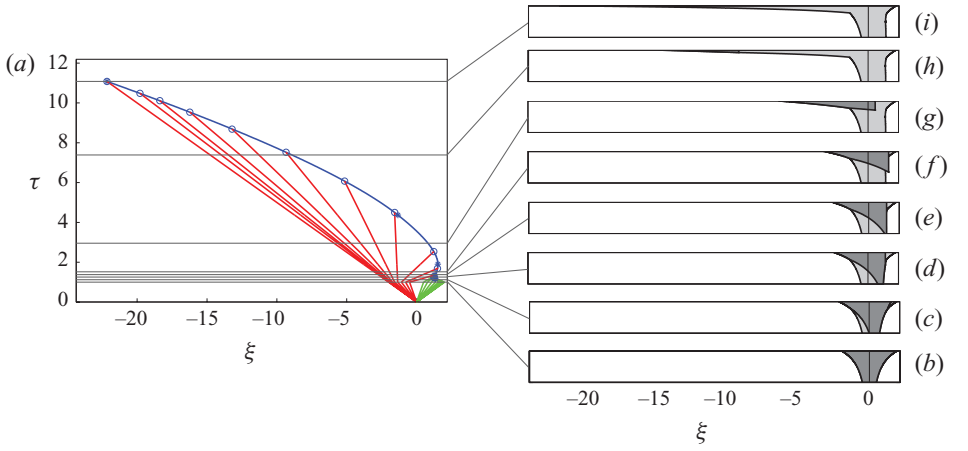

FIGURE 15. (Colour online) Post-injection migration in the negative-slope-with-weak-flow interval with $\mathscr{M} = 2$, $\Gamma = 0.5$, $N_f = 1$ and $N_s = -4$: (*a*) the evolution of the plume in characteristic space with waves of the left and right fronts in red and green, respectively, and the peak and shock paths in blue; (*b*)–(*f*) the shape of the plume at several times during migration, with mobile CO_2 in dark grey, the region containing trapped CO_2 in light grey and groundwater in white.

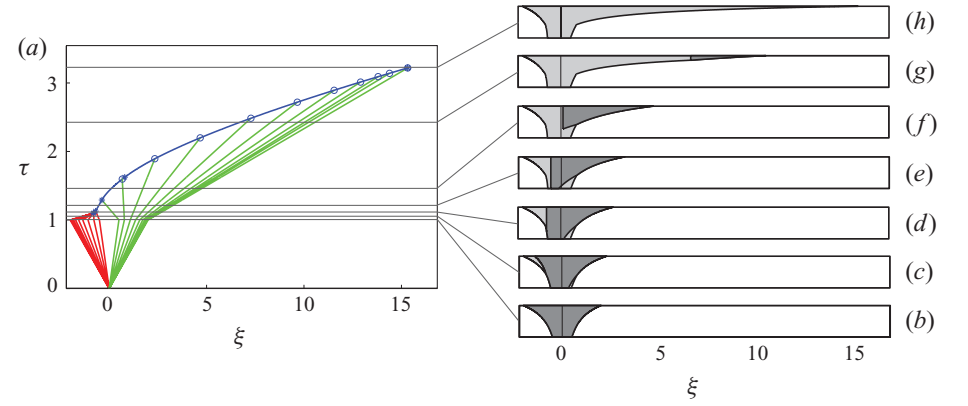

FIGURE 16. (Colour online) Post-injection migration in the positive-slope-with-weak-flow interval with $\mathscr{M} = 2$, $\Gamma = 0.5$, $N_f = 1$ and $N_s = 4$: (*a*) the evolution of the plume in characteristic space with waves of the left and right fronts in red and green, respectively, and the peak and shock paths in blue; (*b*)–(*f*) the shape of the plume at several times during migration, with mobile CO_2 in dark grey, the region containing trapped CO_2 in light grey and groundwater in white.

one has formed, or with ξ_{LR} and then with ξ_{RL} if one has not. Then it must collide with ξ_{RS} and ultimately with ξ_{RR}. As before, it is not tractable to perform further analysis explicitly and we instead use a decision-tree algorithm; however, as before, the process is entirely algebraic.

We illustrate an example of the evolution of the plume in this interval in figure 16; the order of collisions in this example is $\xi_{LL} \to \xi_{LS}$ forming a shock, $\xi_{LR} \to \xi_\sigma$, $\xi_\sigma \to \xi_{RL}$, $\xi_\sigma \to \xi_{RS}$ and $\xi_\sigma \to \xi_{RR}$.

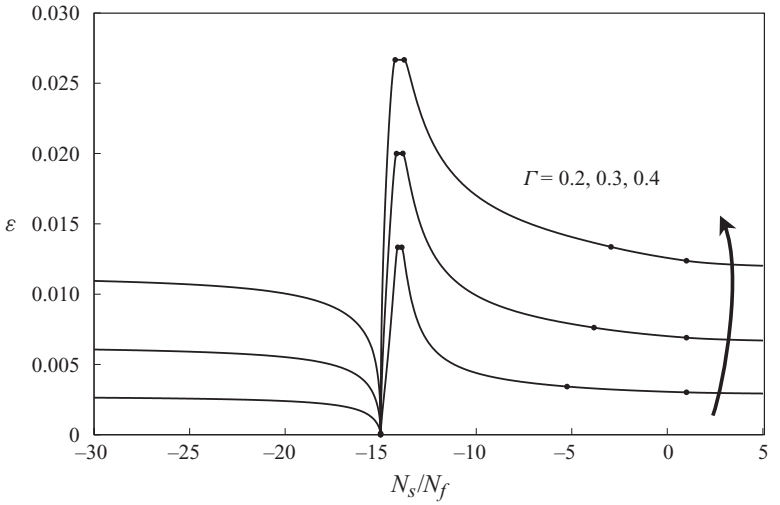

FIGURE 17. Storage efficiency, ε, as a function of N_s/N_f for several values of Γ, as indicated, at $\mathscr{M} = 15$. The black points correspond to the black points on the N_s/N_f line in figure 10. Note that case 5 does not exist for these values of $\mathscr{M}$ and Γ. Case 5 does not introduce any noteworthy features.

4. Plume footprint and storage efficiency

We are primarily interested here in macroscopic measures of the plume evolution. One such measure is the volume of CO_2 stored per unit volume of aquifer 'used'. This is the storage efficiency, an important metric in capacity estimation (Bachu *et al.* 2007). We define the storage efficiency, ε, as

$$\varepsilon = \frac{V_{CO_2}}{V_T} = \frac{Q_i T_i}{H L_T (1 - S_{wc})\phi}, \tag{4.1}$$

where V_{CO_2} is the volume of CO_2 injected and V_T is the total volume of aquifer used; we define V_T to be the total pore volume available for CO_2 storage in a rectangle of thickness H and length L_T, where L_T is the total extent in the x-direction of the fully trapped CO_2 plume (Juanes & MacMinn 2008; Juanes *et al.* 2010). Taking $\xi_T = L_T/L_c$ and using L_c as defined in § 2, we have that

$$\varepsilon = \frac{2}{\xi_T}. \tag{4.2}$$

The storage efficiency takes a value between 0 and Γ, and is inversely proportional to the dimensionless plume footprint, i.e. for a given volume of CO_2 injected, a larger footprint corresponds to less efficient storage.

The storage efficiency can be readily evaluated from the solution to the migration equation as a function of N_s/N_f, $\mathscr{M}$ and Γ, and this can be done quickly and comprehensively over a large range of parameters owing to the analytical nature of the solution. In figure 17, we plot the storage efficiency as a function of N_s/N_f for several values of Γ.

The shape of the storage efficiency curve has several noteworthy features. The storage efficiency drops to exactly zero at $N_s/N_f = -\mathscr{M}$, although in reality plume motion would be arrested by capillarity as the plume becomes very thin. The plateau of highest efficiency is achieved in case 3, where the plume becomes fully trapped before a shock forms: this case is sufficiently simple that the storage efficiency can

be evaluated explicitly, and is given by $\varepsilon_{max} = \Gamma/\mathscr{M}$ for all of case 3. The flow-only efficiency ($N_s/N_f = 0$) is also known explicitly, and is given by $\varepsilon_f = 2\Gamma^2/[\mathscr{M}\Gamma^2 + (2-\Gamma)(\mathscr{M}-(1-\Gamma))]$ (Juanes & MacMinn 2008; Juanes *et al.* 2010). The storage efficiency approaches its slope-only value asymptotically from above or below as N_s/N_f becomes large or small, respectively: this quantity does not have a simple analytical expression, but is given to very good approximation by $\varepsilon_s = \Gamma^2/[0.9\mathscr{M} + 0.49]$. This collection of expressions, used together with knowledge of the qualitative shape of the storage efficiency curves shown in figure 17, is sufficient to quickly and easily estimate the storage efficiency for any particular values of N_s/N_f, $\mathscr{M}$ and Γ.

It is clear that storage efficiency always decreases with $\mathscr{M}$: this is because increasing $\mathscr{M}$ strengthens the 'tonguing' of the plume during both injection and post-injection migration. These long thin layers of CO_2 slow residual trapping and therefore reduce storage efficiency. Similarly, the storage efficiency always increases with Γ: this is because more CO_2 is left behind upon imbibition, and so the plume becomes fully trapped over a shorter migration distance.

5. Conclusions

We have developed a complete solution to a hyperbolic gravity-current model for CO_2 migration in a saline aquifer due to groundwater flow and aquifer slope, subject to residual trapping and accounting for the tongued end-of-injection plume shape. We have shown how the solution changes with N_s/N_f, $\mathscr{M}$ and Γ, and also explored the effect of these parameters on the overall storage efficiency. While the main contribution of this model is the insight it provides into the physics of CO_2 migration and trapping, we illustrate in Juanes *et al.* (2010) and Szulczewski & Juanes (2009) how it can be used to develop basin-specific capacity estimates.

We find that the maximum storage efficiency is achieved for a relatively large negative value of the parameter N_s/N_f, that is, when there is a gentle down-dip groundwater flow. This is a non-trivial result: figure 17 shows that while the storage efficiency is essentially the same for the slope-only, up-dip flow and flow-only cases, a gentle down-dip flow can provide a multiple fold increase in storage efficiency. Hydrogeological conditions leading to this interplay between slope and groundwater flow are known to occur in many continental sedimentary basins (Garven 1995).

Because the areal footprint of the CO_2 plume is very large, it is likely that the plume would encounter faults or fractures as it migrates. While the capillary entry pressure would prevent upwards flow in many cases, it is possible that some CO_2 would leak into overlying formations through larger fractures. Pritchard (2007), Farcas & Woods (2009) and Woods & Farcas (2009), for example, have recently studied leakage in some detail. The impact of leakage in all cases is found to depend strongly on the distribution, permeability and capillary entry pressure of the fractures. These considerations, although relevant to the problem of CO_2 migration, are beyond the scope of this study.

While we have not included the effect of CO_2 dissolution here, it is well known that CO_2 is weakly soluble in groundwater, and therefore both residual CO_2 and CO_2 from the mobile plume will dissolve slowly into the nearby groundwater as the plume migrates. Because the density of groundwater increases with dissolved CO_2 content, the boundary layer of CO_2-saturated groundwater near the mobile plume is unstable. This instability eventually results in so-called convective mixing, where plumes of dense, CO_2-saturated groundwater sink away from the interface as plumes of 'fresh' groundwater rise upwards. It has been shown that for a stationary

plume of CO_2, convective mixing is triggered on time scales that are short relative to required storage times, and that it dramatically increases the rate of CO_2 dissolution compared to diffusive transport alone (Ennis-King & Paterson 2005; Riaz *et al.* 2006). We expect that dissolution will have a non-negligible contribution to overall trapping. In a future study we shall incorporate dissolution into the migration equation and study the importance of dissolution relative to capillary trapping and the impact of dissolution on the storage efficiency.

The work of C.W.M. was partly funded by the Martin Family Society of Fellows for Sustainability. Additional funding was provided by the ARCO Chair in Energy Studies, the Reed Research Fund and the US Department of Energy under grant DE-FE0002041. This financial support is gratefully acknowledged.

REFERENCES

Bachu, S., Bonijoly, D., Bradshaw, J., Burruss, R., Holloway, S., Christensen, N. P. & Mathiassen, O. M. 2007 CO_2 storage capacity estimation: methodology and gaps. *Intl J. Greenhouse Gas Control* **1** (4), 430–443.

Bachu, S., Gunter, W. D. & Perkins, E. H. 1994 Aquifer disposal of CO_2: hydrodynamic and mineral trapping. *Energy Convers. Manage.* **35** (4), 269–279.

Barenblatt, G. I., Entov, V. M. & Ryzhik, V. M. 1972 *Theory of Non-Steady Filtration of Fluids and Gases*. Nedra.

Bear, J. 1972 *Dynamics of Fluids in Porous Media*. Elsevier (reprinted with corrections, Dover, 1988).

Dussan V, E. B. & Auzerais, F. M. 1993 Buoyancy-induced flow in porous media generated near a drilled oil well. Part 1. The accumulation of filtrate at a horizontal impermeable boundary. *J. Fluid Mech.* **254**, 283–311.

Ennis-King, J. & Paterson, L. 2005 Role of convective mixing in the long-term storage of carbon dioxide in deep saline formations. *Soc. Pet. Engng J.* **10** (3), 349–356.

Farcas, A. & Woods, A. W. 2009 The effect of drainage on the capillary retention of CO_2 in a layered permeable rock. *J. Fluid Mech.* **618**, 349–359.

Garven, G. 1995 Continental-scale groundwater flow and geologic processes. *Annu. Rev. Earth Planet. Sci.* **23**, 89–117.

Hesse, M. A., Orr Jr, F. M. & Tchelepi, H. A. 2008 Gravity currents with residual trapping. *J. Fluid Mech.* **611**, 35–60.

Hesse, M. A., Tchelepi, H. A., Cantwell, B. J. & Orr Jr, F. M. 2007 Gravity currents in horizontal porous layers: transition from early to late self-similarity. *J. Fluid Mech.* **577**, 363–383.

Hesse, M. A., Tchelepi, H. A. & Orr Jr, F. M. 2006 Scaling analysis of the migration of CO_2 in saline aquifers. In *SPE Annual Technical Conference and Exhibition (SPE 102796)*, San Antonio, TX.

Huppert, H. E. 1982 The propagation of two-dimensional and axisymmetric viscous gravity currents over a rigid horizontal surface. *J. Fluid Mech.* **121**, 43–58.

Huppert, H. E. & Woods, A. W. 1995 Gravity-driven flows in porous layers. *J. Fluid Mech.* **292**, 55–69.

Juanes, R. & MacMinn, C. W. 2008 Upscaling of capillary trapping under gravity override: application to CO_2 sequestration in aquifers. In *SPE/DOE Symposium on Improved Oil Recovery (SPE 113496),* Tulsa, OK, USA.

Juanes, R., MacMinn, C. W. & Szulczewski, M. L. 2010 The footprint of the CO_2 plume during carbon dioxide storage in saline aquifers: storage efficiency for capillary trapping at the basin scale. *Transp. Porous Media* **82** (1), 19–30.

Juanes, R., Spiteri, E. J., Orr Jr, F. M. & Blunt, M. J. 2006 Impact of relative permeability hysteresis on geological CO_2 storage. *Water Resour. Res.* **42**, W12418.

Kochina, I. N., Mikhailov, N. N. & Filinov, M. V. 1983 Groundwater mound damping. *Intl J. Engng Sci.* **21** (4), 413–421.

Kumar, A., Ozah, R., Noh, M., Pope, G. A., Bryant, S., Sepehrnoori, K. & Lake, L. W. 2005 Reservoir simulation of CO_2 storage in deep saline aquifers. *SPE J.* **10** (3), 336–348.

Lackner, K. S. 2003 Climate change: a guide to CO_2 sequestration. *Science* **300** (5626), 1677–1678.

Lax, P. D. 1972 The formation and decay of shock waves. *Amer. Math. Monthly* **79** (3), 227–241.

MacMinn, C. W. & Juanes, R. 2009 Post-injection spreading and trapping of CO_2 in saline aquifers: impact of the plume shape at the end of injection. *Comput. Geosci.* **13** (4), 483–491.

Nicot, J.-P. 2008 Evaluation of large-scale CO_2 storage on fresh-water sections of aquifers: an example from the Texas Gulf Coast Basin. *Intl J. Greenhouse Gas Control* **2** (4), 582–593.

Nordbotten, J. M. & Celia, M. A. 2006 Similarity solutions for fluid injection into confined aquifers. *J. Fluid Mech.* **561**, 307–327.

Nordbotten, J. M., Celia, M. A. & Bachu, S. 2005 Injection and storage of CO_2 in deep saline aquifers: analytical solution for CO_2 plume evolution during injection. *Transp. Porous Media* **58** (3), 339–360.

Orr Jr, F. M. 2004 Storage of carbon dioxide in geological formations. *J. Pet. Technol.* (9), 90–97.

Pritchard, D. 2007 Gravity currents over fractured substrates in a porous medium. *J. Fluid Mech.* **584**, 415–431.

Pruess, K. & García, J. 2002 Multiphase flow dynamics during CO_2 disposal into saline aquifers. *Environ. Geol.* **42** (2–3), 282–295.

Riaz, A., Hesse, M., Tchelepi, H. A. & Orr Jr, F. M. 2006 Onset of convection in a gravitationally unstable diffusive boundary layer in porous media. *J. Fluid Mech.* **548**, 87–111.

Schrag, D. P. 2007 Preparing to capture carbon. *Science* **315** (5813), 812–813.

Szulczewski, M. & Juanes, R. 2009 A simple but rigorous model for calculating CO_2 storage capacity in deep saline aquifers at the basin scale. *Energy Procedia (Proc. GHGT-9)* **1** (1), 3307–3314.

Verdon, J. & Woods, A. W. 2007 Gravity-driven reacting flows in a confined porous aquifer. *J. Fluid Mech.* **588**, 29–41.

Woods, A. W. & Farcas, A. 2009 Capillary entry pressure and the leakage of gravity currents through a sloping layered permeable rock. *J. Fluid Mech.* **618**, 361–379.

Yortsos, Y. C. 1995 A theoretical analysis of vertical flow equilibrium. *Transp. Porous Media* **18** (2), 107–129.